ACADEMIC
PRESS

Available online at www.sciencedirect.com
SCIENCE DIRECT®

Journal of Computational Physics 184 (2003) 122–148

JOURNAL OF
COMPUTATIONAL
PHYSICS

www.elsevier.com/locate/jcp

Two numerical methods for an inverse problem for the 2-D Helmholtz equation ☆

Yuriy A. Gryazin[a,b,1], Michael V. Klibanov[a], Thomas R. Lucas[a,*]

[a] Department of Mathematics, University of North Carolina at Charlotte, Charlotte, NC 28223, USA
[b] Institute of Computational Technologies, Novosibirsk, 630090, Russia

Received 13 August 2001; received in revised form 30 September 2002

Abstract

Two solution methods for the inverse problem for the 2-D Helmholtz equation are developed, tested, and compared. The proposed approaches are based on a marching finite-difference scheme which requires the solution of an overdetermined system at each step. The preconditioned conjugate gradient method is used for rapid solutions of these systems and an efficient preconditioner has been developed for this class of problems. Underlying target applications include the imaging of land mines, unexploded ordinance, and pollutant plumes in environmental cleanup sites, each formulated as an inverse problem for a 2-D Helmholtz equation. The images represent the electromagnetic properties of the respective underground regions. Extensive numerical results are presented.

Keywords: Helmholtz equation; Elliptic systems method; Subsurface imaging; Land mines; PCG; Preconditioners

---

1. Introduction

In this paper two methods for the solution of a 2-D inverse problem for the Helmholtz equation, with the data originated by frequency sweeps, are presented and compared. An important common feature of both methods is that the original inverse problem is reduced to a set of overdetermined boundary value problems (BVPs) for PDE operators depending on the modulated frequency as a parameter. Because of the overdetermination, the normal solutions of these BVPs are sought. The solution of each of those BVPs via finite differences leads to the solution of a large sparse matrix system. This is one significant difference between the current approach and the majority of previous ones, in which full, rather than sparse matrices were solved, due to the integral, rather than the differential form of the resulting equation for the linearized

---

☆ This research was supported by the US Army Research Office Grant DAAG 55-98-1-0401.

[*] Corresponding author. Tel.: +1-704-687-4571; fax: +1-704-687-6415.
E-mail addresses: gryazin@isu.edu (Y.A. Gryazin), mvklibanv@email.uncc.edu (M.V. Klibanov), trlucas@uncc.edu (T.R. Lucas).
[1] Present address: Department of Mathematics, Idaho State University, Pocatello, ID 83209, USA.

PII: S0021-9991(02)00023-2

inverse problems, cf. [1,4–6]. Because of the resulting sparse positive definite matrix, it is a natural choice to use the preconditioned conjugate gradient method (PCG) to solve it. A version of this method, adapted to the specific problem, is developed here.

In the first algorithm, the H-method introduced for the first time here, the unknown perturbation term is corrected from one iteration to the next, where the iterations are performed with respect to frequency, going from the highest frequency (in the selected frequency band) to the lowest. Finally the perturbation term is recovered at the lowest frequency. This approach is somewhat similar to the propagation–backpropagation method of [20], see also [9]. However, in [20] different emitting angles were considered, unlike in our case of varying frequency. In addition, a certain resulting matrix C_j was replaced by its asymptotic value in [20], because of difficulties in its computation, whereas we calculate all matrices precisely. Interestingly, in [20] a normal solution was also sought. In the second method, the p-method, the unknown coefficient is eliminated from the original PDE by differentiation with respect to frequency. The result is an overdetermined BVP for an integro-differential PDE with Volterra-like integrals with respect to frequency. This idea was proposed and implemented by the authors in [16]. However, we also describe this idea in the current paper (for the sake of reader's convenience), as we want to compare the approach of [16] with the newer method, which has certain advantages over the previous one.

In the PCG method, which is used to find the normal solutions in both of the above methods, the key question involves the selection of a preconditioner. Here the preconditioner will be selected to be the exact factorization of one of the original matrices using the method of nested dissection [12], but only for a small number of frequencies. This selection has been found to work very well for nearby frequencies where it is an excellent approximate inverse. In this approach an automatic algorithm for the near optimal choice of frequency ranges over which the same preconditioner is used has been developed. The average number of iterations of the conjugate gradient method for our final runs for both methods is about 4–5. Because the factored matrix does not depend on the solution of the inverse problem, its factorization could be effectively parallelized, but this expansion of the presented algorithm is not explored in this paper.

The idea of eliminating the unknown perturbation term using differentiation leading to a differential form of the resulting system was explored in our earlier publications (see for example [15] or [19]), in which inverse problems for parabolic equations were considered. This approach was called the Elliptic Systems Method (ESM), because the Volterra-like integrals with respect to time were eliminated via a truncated generalized Fourier series, leading to an overdetermined BVP of the fourth order for a coupled system of elliptic equations, one for each Fourier coefficient. This approach proved to be successful for the accurate locations of the targets, but the values of the unknown coefficients within those targets were imaged poorly. In contrast, in this paper we continue the effort begun in [16] to develop a second generation of the ESM, in which truncated generalized Fourier series are not used. The successful use of the new H-method here leads to a deepened understanding of the ESM, in that the above differentiation which is a principal feature of the p-method [16], is also shown to be unnecessary. In addition the requirement of the loss tangent assumption (Section 2.1) is no longer required.

This paper is motivated by the authors interest in the development of new and effective methods for the imaging of land mines using Ground Penetrating Radar (GPR). Thus, a simplified model of propagation of the GPR signal is presented here. In particular, realistic ranges of parameters are used. The problem of the imaging of land mines is considered as an 2-D inverse problem for the Helmholtz equation with Sommerfeld boundary conditions. The two inverse algorithms developed here should be considered as a first step towards this challenging imaging goal. In order to continue towards this goal, one should incorporate into the model some additional features, such as: (i) a 3-D, rather than the current 2-D model, (ii) a point source, as opposed to the current initializing plane wave, (iii) geometrical irregularities of the air/ground interface, and (iv) measurements displaced from the air/ground interface, etc. The authors hope that these algorithms might provide a basis for these further developments. In addition, this methodology can serve as a base for the imaging of other obscured objects in a variety of applications, including the imaging of unexploded ordinances and pollutant plumes in environmental cleanup sites [9,10]. Land mines are modeled as inclusions of a small size embedded into a known background. A frequency dependent back reflected signal is measured on the air/ground interface. Because the sizes of the targets are small compared with the size of the region of interest, a linearized inverse problem is considered. This is justified by the assumption that the L_2 norms of the targets are small in a certain sense, see Section 2 for details.

2. The forward and inverse problems

2.1. Partial differential equation

The GPR signal is modeled here as a polarized electrical plane wave $E_0 = (0, 0, \exp(\mathrm{i}\omega\sqrt{\mu_0\varepsilon_0} \cdot y)) \cdot \exp(-\mathrm{i}\omega t)$ propagating along the y-direction in the half space $\{y < 0\}$. Here ω is the angular frequency of the signal, $\mu_0 = 4\pi \times 10^{-7}$ Henry/m is the magnetic permeability of free space and $\varepsilon_0 = 8.854 \times 10^{-12}$ Farad/m is the dielectric permittivity of free space. It is assumed that $\{y < 0\}$ is air and $\{y > 0\}$ is ground, where the mine-like targets are located. All functions below depend only on the two spatial variables $(x, y) \equiv \mathbf{x}$. Let $E(\mathbf{x}, \omega) = (0, 0, u(\mathbf{x}, \omega)) \cdot \exp(-\mathrm{i}\omega t)$ be the electric field. Then the following Helmholtz PDE for the function $u(\mathbf{x}, \omega)$ can be derived from Maxwell's system [17]

$$\nabla^2 u + k^2(\mathbf{x}, \omega)u = 0. \tag{2.1}$$

Here the function $k^2(\mathbf{x}, \omega)$ has the form

$$\begin{aligned} k^2(\mathbf{x}, \omega) &= \omega^2\mu_0\varepsilon(\mathbf{x}) + \mathrm{i}\omega\mu_0\sigma(\mathbf{x}, \omega) \quad \text{or} \\ &= \omega^2\mu_0\varepsilon(\mathbf{x})\left(1 + \frac{\mathrm{i}\sigma(\mathbf{x}, \omega)}{\omega\varepsilon(\mathbf{x})}\right), \end{aligned}$$

where $\varepsilon(\mathbf{x})$ and $\sigma(\mathbf{x}, \omega)$ are, respectively, the electrical permittivity and the electrical conductivity of the medium. It is also assumed that $\varepsilon \equiv \varepsilon_0$ in air. Let $\varepsilon(\mathbf{x}) = \varepsilon_\mathrm{r}(\mathbf{x})\varepsilon_0$, where ε_r is the relative dielectric constant. In air $\varepsilon_\mathrm{r}(\mathbf{x}) \equiv 1$ and $\sigma(\mathbf{x}, \omega) \equiv 0$. Now introduce the so-called "loss tangent" as [17]

$$\tan(\delta) = \frac{\sigma(\mathbf{x}, \omega)}{\omega\varepsilon(\mathbf{x})}. \tag{2.2}$$

Then

$$k^2 = \omega^2\mu_0\varepsilon_r\varepsilon_0(1 + \mathrm{i}\tan(\delta)). \tag{2.3}$$

In this paper it is assumed that the loss tangent does not depend on ω, i.e. $(\partial/\partial\omega)[\tan(\delta)] = 0$, at least in the frequency domains of interest. This condition is a requirement for the integro-differential method originally introduced in [16] (which is referred to in this paper as the p-method) but not for the more general iterative correction algorithm introduced in this paper which is referred as the H-method, although a detailed development of this extension will not be presented in this paper. This loss tangent assumption is satisfied with sufficient accuracy in many practical scenarios of land mine detection, as can be seen from the data in [7].

2.2. Parameter ranges

It is useful first to establish the parameter ranges for the PDE (2.1). All units below are given in the SI system. The frequency of the signal $f = \omega/2\pi$ is between 0.5 and 3 GHz, i.e., $f \in (0.5, 3) \times 10^9\,\mathrm{s}^{-1}$. The approximate values of the parameters ε_r, $\tan(\delta)$, k^2, k, and the wavelength $\lambda = 2\pi/\mathrm{Re}(k)$ for different soil moistures as well as for trinitrotoluene (TNT) are given in Table 1 for the frequency $f = 1\,\mathrm{GHz}$. In this table the data of [7] is used.

In Section 5 targets filled with TNT will be considered in a background of wet soil with the GPR signal first propagating through air.

At $f = 3\,\mathrm{GHz}$, the wavelength λ is less by about a factor of 3, whereas at $f = 0.5\,\mathrm{GHz}$, λ nearly doubles, as compared with its values in this table. Therefore,

$$\lambda \in \begin{cases} (5,35)\,\mathrm{cm} & \text{in the ground,} \\ (10,60)\,\mathrm{cm} & \text{in the air.} \end{cases} \tag{2.4}$$

This range of wavelengths significantly affects the grid size in the Finite Difference (FD) solution for both the forward and inverse problems. In order to calculate the forward problem accurately, one should use at least 10 grid points per wavelength. Suppose, for example, that one wants to calculate the function u in a square region of size $2\,\mathrm{m} \times 2\,\mathrm{m}$. Then because of (2.4), this would mean that one should use at least a 400×400 grid for $\lambda = 5\,\mathrm{cm}$. This motivated the development of a new efficient algorithm for the solution of the Helmholtz equation with complex variable coefficients [14]. Below all data simulations for the inverse problems (through solutions of forward problems) are computed by the method of [14].

2.3. Statement of the forward problem

It will be assumed that the electrical parameters ε and σ have constant background values everywhere in the ground, except in the mine-like targets, whose sizes are small compared with the size of the region of interest. Let $k_0 = k_0(y,\omega)$ be the function k in (2.3) for the background medium. Then this function has a discontinuity on the air/ground interface,

$$k_0^2 = \begin{cases} \omega^2\mu_0\varepsilon_0 & \text{for } y < 0, \\ \omega^2\mu_0\varepsilon_r\varepsilon_0[1 + \mathrm{i}\tan(\delta)] & \text{for } y > 0. \end{cases} \tag{2.5a}$$

Let $u_0 = u_0(y,\omega)$ be the solution of the PDE (2.1), which corresponds to the initial plane wave without targets present. Then u_0 consists of the initial, reflected, and transmitted plane waves [17],

$$u_0 = \begin{cases} \mathrm{e}^{\mathrm{i}k_0 y} + R(k_0)\mathrm{e}^{-\mathrm{i}k_0 y} & \text{for } y < 0, \\ T(k_0)\mathrm{e}^{\mathrm{i}k_0 y} & \text{for } y > 0, \end{cases} \tag{2.5b}$$

where $R(k_0)$ and $T(k_0)$ are the reflection and transmission coefficients given by

$$R(k_0) = \frac{k_0^- - k_0^+}{k_0^- + k_0^+}, \quad T(k_0) = \frac{2k_0^-}{k_0^- + k_0^+}. \tag{2.5c}$$

Table 1
Approximate values of ε_r, $\tan(\delta)$, k^2, k, and λ for different soil moistures and TNT at $f = 1\,\mathrm{GHz}$

Medium	ε_r	$\tan(\delta)$	k^2 (m^{-2})	k (m^{-1})	λ (cm)
Air	1	0	439.2	20.9	30
Dry soil	2.9	0.025	$1273 + \mathrm{i}31$	$35.7 + \mathrm{i}0.43$	17
Wet soil, 5% moisture	4	0.22	$1756 + \mathrm{i}395$	$42 + \mathrm{i}4.7$	15
TNT	2.86	0.0018	$1256 + \mathrm{i}2.26$	$35.4 + \mathrm{i}0.03$	17.7

Here k_0^- and k_0^+ are the values of k_0 for $y < 0$ and $y > 0$, respectively. The presence of these coefficients ensures the continuity of the function u_0 together with its first derivatives at $\{y = 0\}$.

A solution of the Eq. (2.1) will be sought in the form $u = u_0 + v$, where the function $v(\mathbf{x}, \omega)$ represents the wave scattered by mine-like targets with compact supports in $\mathbb{R}^2_+ = \{y > 0\}$. Hence, v satisfies the PDE:

$$\nabla^2 v + k^2 v = -\left(k^2 - k_0^2\right) u_0, \quad \mathbf{x} \in \mathbb{R}^2, \tag{2.6}$$

where $k^2 = k_0^2$ outside of the targets. In addition, Sommerfeld radiation boundary conditions will be imposed at infinity

$$\lim_{r \to \infty} \sqrt{r} \left(\frac{\partial v}{\partial r} - \mathrm{i} k_0 v \right) = 0, \tag{2.7}$$

where $r = \sqrt{x^2 + y^2}$, $\mathrm{Im}(k_0) > 0$ and the limit holds uniformly in all directions. Eqs. (2.6) and (2.7) specify the forward problem including the discontinuity in the refractive index at $\{y = 0\}$. It was shown in ([4], Proposition A.1.3) that a 3-D analog of the forward problem (2.6), (2.7) has an unique solution in a certain Sobolev space. This leads us to assume throughout this paper that a similar result is valid in the 2-D case.

It is natural to consider in practical computations a bounded domain G_L, which is obtained by a cut-off of the infinite space $\mathbb{R}^2$. Here G_L will be taken to be the square $G_L = \{|x|, |y| \leqslant L\}$, and the solution will be carried out using the approach developed by the authors in [14]. In this case the condition (2.7) is replaced with the Sommerfeld-like boundary conditions

$$v_x \mp \mathrm{i} k_0 v|_{x = \pm L} = 0, \quad v_y \mp \mathrm{i} k_0 v|_{y = \pm L} = 0. \tag{2.8}$$

It was shown numerically in [14] that if the targets are located "well within" the square G_L (i.e., far from the boundaries), then, for the parameter ranges listed in Table 1, the resulting values of the function $v(\mathbf{x}, \omega)$ for points $\mathbf{x}$ located near the air/ground interface $\{y = 0\}$ are independent of L for $L \geqslant 53$ cm. For this reason, for the solution of the *inverse* problem will be carried out over a smaller domain $\Omega \subset G_L$, $\Omega \subset \mathbb{R}^2_+$. First data $v|_{y=0}$ and $v_y|_{y=0}$ for the inverse problem using the solution of the forward problem in the domain G_L with $L = 1.5$ m is generated. Next, to solve the inverse problem the domain

$$\Omega = \{\mathbf{x} = (x, y) : |x| < L_1 = 0.6\,\mathrm{m},\ 0 < y < L_2 = 0.4\,\mathrm{m}\}$$

will be used. In doing this, the following boundary conditions for the function v on the side and top boundaries of the domain Ω will be used:

$$v_x \mp \mathrm{i} k_0 v|_{x = \pm L_1} = 0, \tag{2.9a}$$

$$v_y - \mathrm{i} k_0 v|_{y = L_2} = 0. \tag{2.9b}$$

2.4. Statement of the inverse problem

Let ε_1 and $\tan(\delta_1)$ be the values of the parameters ε and $\tan(\delta)$ everywhere in the ground, except for the mine-like targets. Then

$$\varepsilon(\mathbf{x}) = \varepsilon_1 + h_\varepsilon(\mathbf{x}), \quad \tan(\delta) = \tan(\delta_1) + h_\sigma(\mathbf{x}), \tag{2.10}$$

where the perturbations $h_\varepsilon(\mathbf{x})$ and $h_\sigma(\mathbf{x})$ are due to the presence of the mine-like targets. Hence, the determination of these functions would yield both the locations of these targets and the values of the electrical parameters within them. For the sake of convenience, a perturbation $h(\mathbf{x})$ of the background coefficient $k_0^2(\mathbf{x}, \omega)$ as a "whole" will be introduced:

$$h(\mathbf{x}) = \frac{k^2(\mathbf{x},\omega) - k_0^2(\mathbf{x},\omega)}{k_0^2(\mathbf{x},\omega)}. \tag{2.11}$$

Hence,

$$k^2(\mathbf{x},\omega) = k_0^2[1 + h(\mathbf{x})] \tag{2.12a}$$

$$= \omega^2 k_{0s}^2(x)[1 + h(\mathbf{x})], \tag{2.12b}$$

where $k_{0s}(\mathbf{x}) = k_0(\mathbf{x},\omega)/\omega$. The perturbation function $h(\mathbf{x})$ is independent of ω because of the loss tangent assumption that $(\partial/\partial\omega)[\tan(\delta)] = 0$. By (2.10)–(2.12b) the function $h(\mathbf{x})$ can be obtained from the functions $h_\varepsilon(\mathbf{x})$ and $h_\sigma(\mathbf{x})$ through the following transformation:

$$h = \frac{h_\varepsilon + \mathrm{i}[\varepsilon_1 h_\sigma + h_\varepsilon \tan(\delta_1) + h_\varepsilon h_\sigma]}{\varepsilon_1[1 + \mathrm{i}\tan(\delta_1)]}.$$

Once the complex-valued function $h(\mathbf{x})$ has been obtained from the solution of the inverse problem, the perturbations of the physical parameters can be recovered by using the formulas:

$$h_\varepsilon = \varepsilon_1[\mathrm{Re}(h) - \tan(\delta_1)\cdot \mathrm{Im}(h)],$$

$$h_\sigma = \frac{\mathrm{Im}(h)\cdot[1 + \tan^2(\delta_1)]}{1 + \mathrm{Re}(h) - \tan(\delta_1)\cdot\mathrm{Im}(h)}.$$

Inverse problem. *Determine the perturbation function* $h(\mathbf{x})$, *given the functions* $\varphi(x,\omega)$, $\psi(x,\omega)$ defined as

$$\varphi(x,\omega) = v|_{y=0}, \tag{2.13a}$$

$$\psi(x,\omega) = v_y|_{y=0} \tag{2.13b}$$

for $x \in (-L_1, L_1)$, $\omega \in (\omega_{\min}, \omega_{\max})$.

The measurements are performed at points on a certain interval $(-L_1, L_1)$ of the line $\{y = 0\}$ located on the air/ground interface and at discrete frequencies $\omega \in (\omega_{\min}, \omega_{\max})$, by solution of a series of forward problems, one for each frequency. One way to evaluate the normal derivative ψ in (2.13b) given φ would be to solve the boundary value problem (2.6), (2.9a), (2.9b), (2.13a) in the air, i.e. for $\{y < 0\} \cap \{|x| < L_1\}$, where no targets are present, but for purposes of this study we simply evaluate it along with φ, adding Gaussian noise.

The resulting PDE for the function v is

$$\nabla^2 v + k_0^2 v + k_0^2 h(\mathbf{x}) v = -k_0^2 u_0 h(\mathbf{x}), \tag{2.14}$$

where $h(\mathbf{x})$ is a bounded function with compact support in Ω and the function u_0 is given by (2.5b) (for $y > 0$). It will be assumed that the medium of interest, Ω, is basically homogeneous, except for a few mine-like targets whose sizes are small compared with the size of Ω. This suggests the related assumption that also $\|h\|_{L_2(\Omega)} \ll \|s\|_{L_2(\Omega)}$, where the function $s(\mathbf{x}) \equiv 1$. Note that the function v in (2.14) depends nonlinearly on the function h. Hence, linearization leads to dropping the $h(\mathbf{x})v$ term in (2.14). This approach was used previously in a similar context in the publications [15,16,19] of the authors. Using (2.5b) to substitute for u_0, gives the linearized PDE as:

$$\nabla^2 v + k_0^2 v = -k_0^2 T(k_0) \mathrm{e}^{\mathrm{i}k_0 y} h(\mathbf{x}), \quad x \in \Omega \tag{2.15}$$

with the boundary conditions (2.9a), (2.9b), (2.13a), and (2.13b). It should be noted that (2.15) is a PDE with *two* unknown functions, $h(\mathbf{x})$ and $v(\mathbf{x},\omega)$, and *two* boundary conditions $v = \varphi(x,\omega)$ and $v_y = \psi(x,\omega)$ along the side $y = 0$, for many values of ω.

The function $h(x)$ in (2.15) may be isolated by dividing both sides by $k_0^2T(k_0)e^{ik_0y}$. Introduce the new function $H(\mathbf{x},\omega)$ as

$$H(\mathbf{x},\omega)=\frac{v}{k_0^2T(k_0)e^{ik_0y}}. \tag{2.16}$$

Then (2.15) becomes

$$\nabla^2H+2ik_0H_y=-h(\mathbf{x}),\quad x\in\Omega \tag{2.17}$$

with the corresponding derived boundary conditions:

$$H|_{y=0}=\widetilde{\varphi}(x,\omega);\quad H_y|_{y=0}=\widetilde{\psi}(x,\omega);\quad H_x\mp ik_0H|_{x=\pm L_1}=0,\qquad \omega\in(\omega_{\min},\omega_{\max}), \tag{2.18a}$$

$$H_y|_{y=L_2}=0. \tag{2.18b}$$

3. Two inverse algorithms

In this section two novel iterative algorithms for approximating the above inverse problem in a best fit sense are developed. In order to simulate data for the inverse problem, we begin in both cases with a series of finite difference (FD) solutions to the forward problem (2.6)–(2.8) using the solution method developed in [14], over a set of discrete frequencies. The values $\varphi(x,\omega)=v(x,0,\omega)$ and $\psi(x,\omega)=v_y(x,0,\omega)$ are available from the above forward solutions at the computational grid points over the set of discrete frequencies and were used to evaluate $\widetilde{\varphi}(x,\omega)$ and $\widetilde{\psi}(x,\omega)$. Then multiplicative Gaussian noise was added to both $\widetilde{\varphi}$ and $\widetilde{\psi}$ with $\sigma=0.10$ (i.e., 10% noise level) in $\widetilde{\varphi}$ and $\widetilde{\psi}$. The mathematical expectation of this noise is zero. A C^2 cubic spline smoothing process in ω, following de Boor [2], was applied to $\widetilde{\varphi}(x,\omega)$ and $\widetilde{\psi}(x,\omega)$. In this approach the spline coefficients are calculated using a functional, that includes the squares of the deviations of the spline from the noisy data and L_2 norms of the second derivative of the spline. Minimization of this functional establishes a compromise between the requirement of staying close to the given data and obtaining a smooth function. The spatial computational grid for the inverse solver has in general no relationship to the computational grid used in the above forward solver except that the air–soil interface line is common to both. Thus no grid crimes are committed. For a given frequency ω, $\widetilde{\varphi}(x,\omega)$ and $\widetilde{\psi}(x,\omega)$ are first evaluated by this smoothed cubic spline at surrounding forward grid node points $x_{i-1}\leqslant x\leqslant x_i$, then evaluated at x by linear interpolation. This procedure gives $\widetilde{\varphi}$ and $\widetilde{\psi}$ as continuous functions of x and ω, piecewise linear in x and piecewise cubic in ω. Details and illustrative graphs for two different target applications are presented in Section 5.

A common feature of both algorithms is that they involve a series of frequency sweeps in which a sequence of overdetermined BVPs are solved from $\omega_{\max}$ to $\omega_{\min}$. A linear least squares fit of the overdetermined equations for the FD discretized form of this BVP is evaluated at each step. A major difference between these methods, is that the first one corrects the perturbation term at each frequency step by a sort of "back-propagation" approach, whereas in the second the unknown perturbation term is originally eliminated through differentiation with respect to frequency, leading to the solution of an integro-differential PDE, in which integration is carried out with respect to frequency. An approximation to the perturbation term is recovered at the end of this process. In later frequency sweeps, the restart for the second method uses the result of a calculation using the recovered perturbation term. Both methods are stopped when the maximal magnitude of h decreases, the fluctuations increase, or when the change is sufficiently small.

In each of the algorithms a matrix system, which can be written in abstract form as $(B_j^*B_j)(f_j)=(B_j^*K_j)(g_j)$, is to be solved for each iteration step j. Here B_j is a finite difference analog of the elliptic operator $\nabla^2 + 2ik_0\partial/\partial y$ in (2.17) at $\omega = \omega_j$ with the boundary conditions (2.18a) and (2.18b), K_j is certain matrix operator, g_j is a known vector, and vector f_j is unknown. For the case where an analog of the boundary data (2.18a), (2.18b) was given on the entire boundary $\partial\Omega$ (rather than on only a part, as in the current case) convergence of a very similar process was proven in Section 5.1 of [16]. This result offers a heuristic argument suggesting convergence for both of the algorithms of this section.

It was proven in [16] that the recovery of the 4th derivatives with respect to x and y of an analog of f_j was stable. This is supportive of the stability of the computation of the first and second derivatives of the function H, which we compute to recover the perturbation term h, as per (2.17). Other viewpoints also lead us to the same conclusion, in additional to our considerable numerical experience: for example there is a long history in the use of Alternating Directions Implicit methods that shows that when later calculations evaluate finite differences using the same intermediate solutions used in their development, results are stable, but otherwise not [3]. It should be noted that three different regularizing procedures are applied. First, the noise in the data is smoothed using a C^2 cubic spline smoothing process (Section 5.2). Second, all frequencies higher than $\omega_{\max}$ are cut-off. Finally, the discretization and its iterations are another important regularizing tool.

3.1. Discretization method

The physical domain for the inverse problem is selected to be $[-L_x, L_x] \times [0, L_y]$. In the discretization of the PDE second order centered finite-difference approximations are used, with a uniform mesh of size $\Delta x \times \Delta y$, where $\Delta x = 2L_x/M_x$, $\Delta y = L_y/M_y$ with M_x, M_y being the numbers of grid points in the x and y directions, respectively. The boundary conditions are imposed by use of second order correct formula centered on each boundary, using fictitious values outside of Ω. A uniform frequency step of $\Delta\omega = (\omega_{\max} - \omega_{\min})/N$, where N is the number of frequency intervals, is used to partition the interval $[\omega_{\min}, \omega_{\max}]$ into $n-1$ subintervals: $\omega_{\min} = \beta_n < \beta_{n-1} < \cdots < \beta_1 = \omega_{\max}$. The spatially gridded region uses x values over the interval $[-L_x + \Delta x/2, L_x - \Delta x/2]$ and y values over $[\Delta y/2, L_y - \Delta y/2]$ plus the added fictitious points. The alternative gridding method which places grid points directly on the boundary would be expected to give similar results, but has not been explored here.

3.2. First inverse algorithm (H-method)

The inverse problem will be solved by the following: let $B(\omega)$ be the FD-based matrix representing the left-hand sides of Eqs. (2.17), (2.18a), and (2.18b) as a function of ω. It is important to note that $B(\omega)$ depends only on ω, k_0, and the spatial grid. Also, let $S^H(\omega, \overline{h}, \widetilde{\varphi}, \widetilde{\psi})$ be the FD operator for the right-hand sides of (2.17), (2.18a), and (2.18b). S^H depends not only on ω, k_0, and the spatial grid but also on a grid function $\overline{h}$ and of course the overdetermined boundary data $\widetilde{\varphi}$ and $\widetilde{\psi}$ evaluated at the interface grid points. Then on step j solve the overdetermined linear system

$$B(\beta_j)\overline{H}^j = S^H\left(\beta_j, \overline{h}, \widetilde{\varphi}, \widetilde{\psi}\right), \tag{3.1}$$

where the vector $\overline{H}^j$ represents the FD approximation to the grid values of $H(\mathbf{x}, \beta_j)$, given $\overline{h}$. Note that the system (2.17), (2.18a), and (2.18b) gives one equation for each spatial grid point, plus one additional equation for each grid point along the air–soil interface $y = 0$. Once $\overline{H}^j$ has been evaluated, one can exploit the fact that it is only an approximate solution to the overdetermined system (3.1), to again use (2.17) to compute an improved value of $\overline{h}$, as

$$\overline{h} := -\left(\nabla^2\overline{H}^j + 2ik_0(\omega)\overline{H}^j_y\right)\Big|_{\omega=\beta_j}, \tag{3.2}$$

where the differential operators are understood in terms of finite differences. This process can be applied $k \geqslant 1$ times for each value of j, always using the latest update of $\overline{h}$.

The complete algorithm for the H-method can now be stated as follows: Initialize $\overline{h}$ to be the zero vector. Then complete a series of sweeps (beginning each new sweep with the latest value of $\overline{h}$ from the previous sweep) as follows until the stopping criteria are satisfied.

For $j = 1, \dots, n$:

I. Solve the overdetermined linear least squares problem (3.1) for $\overline{H}^j$ using the latest value of $\overline{h}$.
II. Evaluate $\overline{H}^j_y$ from $\overline{H}^j$ using FD.
III. Use (3.2) at $\omega = \beta_j$ to compute the updated value for $\overline{h}$ from $\overline{H}^j$ and $\overline{H}^j_y$.
IV. Repeat I–III $k \geqslant 1$ times.

The normal equations method is used to solve the overdetermined linear system (3.1). An alternative approach would have been to use the *QR* decomposition of A [13], which while more robust would have been considerably more time consuming both because of the increased effort required by the direct decomposition and the absence of iterative alternatives. As it stands, (3.1) is essentially a 5-banded matrix system. Applying the normal equations method, involves multiplying both sides of the matrix system (3.1) by the conjugate transpose of $B(\beta_j)$. This gives the square 13-band system

$$B^*(\beta_j)B(\beta_j)\overline{H}^j = B^*(\beta_j)S^H\left(\beta_j, \overline{h}, \widetilde{\varphi}, \widetilde{\psi}\right), \tag{3.3}$$

which is clearly invertible since the columns of the original matrix $B(\beta_j)$ are linearly independent. In fact the new matrix $B^*(\beta_j)B(\beta_j)$ is Hermitian positive definite. This family of equations involves a series of sweeps with slowly changing values of $\omega = \beta_j$, and one or more inner iterations for each value of j.

In Section 4 an iterative solution method based on the preconditioned conjugate gradient method is developed that specifically exploits this structure.

3.3. Second inverse algorithm (p-method)

The second inverse method studied here was originally introduced by the authors in [16]. The two methods are similar in their use of sweeps to progressively improve the grid function $\overline{h}$, their use and treatment of overdetermined boundary conditions and many details of their implementation. The major difference between them is in their treatment of the important difficulty in solving the PDE (2.17): that it consists of one equation with *two* unknown functions $h(\mathbf{x})$ and $v(\mathbf{x}, \omega)$. A principal idea of the ESM in the past has been to eliminate the perturbation term $h(\mathbf{x})$ by differentiation of the original PDE with respect to a parameter on which $h(\mathbf{x})$ does not depend, and then later to recover $h(\mathbf{x})$ by use of the original PDE. The parameter is ω in this case. It will be observed that the new difficulty is that the resulting equation becomes an integro-differential equation, rather than a conventional PDE, which is complicated by requiring an approximate value of $H(\mathbf{x}, \omega)$ for some value of ω.

Following this approach, differentiate (2.17) with respect to ω eliminating $h(\mathbf{x})$. Let

$$p(\mathbf{x}, \omega) = \frac{\partial H}{\partial \omega}. \tag{3.4}$$

As discussed in more detail in [16], it is assumed that for every $x \in \Omega$

$$\lim_{\omega \to \infty} H(\mathbf{x}, \omega) = 0 \tag{3.5}$$

and

$$p, p_y \in L_1(\omega_{\min}, \infty) \tag{3.6}$$

as functions of ω. In the work that follows the working assumption is made that conditions (3.5) and (3.6) hold. Hence,

$$H(\mathbf{x},\omega) = -\int_{\omega}^{\infty} p(\mathbf{x},\tau)\,\mathrm{d}\tau \tag{3.7a}$$

$$= -\int_{\omega}^{\omega_{\max}} p(\mathbf{x},\tau)\,\mathrm{d}\tau + H(\mathbf{x},\omega_{\max}). \tag{3.7b}$$

Eqs. (3.7a) and (3.7b) leads to the result that for $\widehat{H}(\mathbf{x}) \approx H(\mathbf{x},\omega_{\max})$, and $\widehat{H}_y(\mathbf{x}) \approx H_y(\mathbf{x},\omega_{\max})$

$$H(\mathbf{x},\omega) \approx -\int_{\omega}^{\omega_{\max}} p(\mathbf{x},\tau)\,\mathrm{d}\tau + \widehat{H}(\mathbf{x}), \tag{3.8a}$$

$$H_y(\mathbf{x},\omega) \approx -\int_{\omega}^{\omega_{\max}} p_y(\mathbf{x},\tau)\,\mathrm{d}\tau + \widehat{H}_y(\mathbf{x}). \tag{3.8b}$$

For notational convenience the "$\approx$" in (3.8a) and (3.8b) will be replaced with "$=$" in later references.

Let $g_1(x,\omega) = (\partial/\partial\omega)\widetilde{\varphi}(x,\omega)$ and $g_2(x,\omega) = (\partial/\partial\omega)\widetilde{\psi}(x,\omega)$. Because $\widetilde{\varphi}(x,\omega)$ and $\widetilde{\psi}(x,\omega)$ are given by cubic splines in ω, their derivative with respect to ω is trivially evaluated from the spline derivative. Recalling that $k_0(\mathbf{x},\omega) = \omega k_{0s}(\mathbf{x})$, note that differentiating (2.17), (2.18a), and (2.18b) by ω and using (3.7a)–(3.8b), leads to the system:

$$\nabla^2 p + 2\mathrm{i}\omega k_{0s}(\mathbf{x})p_y = 2\mathrm{i}k_{0s}(\mathbf{x})\left[\int_{\omega}^{\omega_{\max}} p_y(\mathbf{x},\tau)\,\mathrm{d}\tau - \widehat{H}_y(\mathbf{x})\right], \quad \mathbf{x}\in\Omega, \tag{3.9a}$$

$$p|_{y=0} = g_1(x,\omega), \quad p_y|_{y=0} = g_2(x,\omega), \quad p_y|_{y=L_2} = 0, \tag{3.9b}$$

$$p_x \mp \mathrm{i}\omega k_{0s}(\mathbf{x})p|_{x=\pm L_1} = \mp \mathrm{i}k_{0s}(\mathbf{x})\left[\int_{\omega}^{\omega_{\max}} p(\mathbf{x},\tau)\,\mathrm{d}\tau - \widehat{H}(\mathbf{x})\right]\Bigg|_{x=\pm L_1}. \tag{3.9c}$$

Thus, we have obtained the boundary value problem (3.9a)–(3.9c) for the integro-differential equation (3.9a) with Volterra-like integrals being present in both the equation itself and the left and right boundary conditions.

Again let $B(\omega)$ be the FD-based matrix representing the left-hand sides of Eqs. (2.17), (2.18a), and (2.18b) as in the previous subsection. Consider the grid valued functions $\overline{H}^1$, $\overline{H}_y^1$, $\overline{p}^j$, $\overline{p}_y^j$, $\overline{k}_{0s}$, and $\overline{h}$, where for example $\overline{p}^j$ and $\overline{k}_{0s}$ represent the grid values of $p(\mathbf{x},\beta_j)$ in its current approximation, $1 \leqslant j \leqslant n$, and $k_{0s}(\mathbf{x})$. To solve (3.9a)–(3.9c), begin with $\omega = \beta_1 = \omega_{\max}$. Initialize $\overline{h}$ to be zero, and solve the overdetermined system (3.1) for $\overline{H}^1$ as in the H-method, using (3.3). Evaluate $\overline{H}_y^1$ from $\overline{H}^1$ by centered finite differences. Now solve the overdetermined system (3.9a), (3.9b), (3.9c) in its FD formulation for $\overline{p}^1$ by the normal equations method using the least squares matrix $B^*(\omega_{\max})B(\omega_{\max})$ and a right-hand side derived from (3.9a)–(3.9c), noting that the two integrals evaluate to zero. For the cases where $j > 1$, the two integrals in (3.9a) and (3.9c) are approximated by the trapezoid rule. Thus

$$\int_{\beta_j}^{\omega_{\max}=\beta_1} \overline{p}(\tau)\,\mathrm{d}\tau \approx \Delta\omega\left[\frac{\overline{p}^j}{2} + \sum_{l=2}^{j-1}\overline{p}^l + \frac{\overline{p}^1}{2}\right] \quad \text{and} \quad \int_{\beta_j}^{\omega_{\max}=\beta_1} \overline{p}_y(\tau)\,\mathrm{d}\tau \approx \Delta\omega\left[\frac{\overline{p}_y^j}{2} + \sum_{l=2}^{j-1}\overline{p}_y^l + \frac{\overline{p}_y^1}{2}\right]. \tag{3.10}$$

Eqs. (3.9a), (3.9b), (3.9c), and (3.10) lead to an overdetermined linear system for $\overline{p}^j$, $j > 1$ at $\omega = \beta_j$:

$$\nabla^2\overline{p}^j + 2\mathrm{i}\left(\omega - \frac{\Delta\omega}{2}\right)\overline{k}_{0s}\overline{p}_y^j = 2\mathrm{i}\overline{k}_{0s}\left[\Delta\omega\sum_{l=2}^{j-1}\overline{p}_y^l + \Delta\omega\frac{\overline{p}_y^1}{2} - \overline{H}_y^1\right], \tag{3.11a}$$

$$\overline{p}^j|_{y=0} = g_1(x,\omega), \quad \overline{p}^j_y|_{y=0} = g_2(x,\omega), \quad \overline{p}^j_y|_{y=L_2} = 0, \tag{3.11b}$$

$$\overline{p}^j_x \mp \mathrm{i}\left(\omega - \frac{\Delta\omega}{2}\right)\overline{k}_{0s}\overline{p}^j|_{x=\pm L_1} = \pm \mathrm{i}\overline{k}_{0s}\left[\Delta\omega\sum_{l=2}^{j-1}\overline{p}^l + \Delta\omega\frac{\overline{p}^1}{2} - \overline{H}^1\right]. \tag{3.11c}$$

Note that (3.11a)–(3.11c) can be extended to the case $j = 1$, by letting $\Delta\omega = 0$, since the integral is zero in this case. Let $S^{p,j}(\omega, \Delta\omega, \overline{k}_{0s}, g_1, g_2, \overline{p}^1, \overline{p}^2, \ldots, \overline{p}^{j-1}, \overline{H}^1, \overline{H}^1_y)$ be the FD operator for the right-hand sides of (3.11a)–(3.11c). $S^{p,j}$ depends also on the spatial grid plus the previous $\overline{p}$ vectors. The ω term is required to evaluate g_1 and g_2. The terms $\overline{H}^1$ and $\overline{H}^1_y$ are determined by the initial approximation for $\overline{h}$, as described above. Thus expressed in matrix form, (3.11a)–(3.11c) becomes:

$$B\left(\beta_j - \frac{\Delta\omega}{2}\right)\overline{p}^j = S^{p,j}(\beta_j, \Delta\omega, \overline{k}_{0s}, g_1, g_2, \overline{p}^1, \overline{p}^2, \ldots, \overline{p}^{j-1}, \overline{H}^1, \overline{H}^1_y). \tag{3.12}$$

The system (3.12) gives one equation for each spatial grid point, plus one additional equation for each grid point along the air–soil interface $y = 0$. As previously in (3.3) the overdetermined system (3.12) will be solved by the normal equations method. Note that the resulting Hermitian positive definite matrix system $B^*(\omega)B(\omega)\overline{p}^j = B^*(\omega)S^{p,j}$ as a function of ω will be identical to that obtained earlier, the difference being in the right-hand sides and the frequency ω at which B is to be evaluated.

The complete algorithm for the p-method can now be stated. Initialize $\overline{h}$ to be the zero vector. Then for each sweep, loop as follows until the stopping criteria are satisfied:

I. Evaluate $\overline{H}^1$ and $\overline{H}^1_y$ from the latest value of $\overline{h}$ using (3.3) for $\omega = \omega_{\max}$.

II. Solve (3.11a)–(3.11c) for p^1, for $\omega = \omega_{\max}$ using $B^*(\omega_{\max})B(\omega_{\max})\overline{p}^1 = B^*(\omega_{\max})S^{p1}(\omega_{\max}, \Delta\omega = 0, \overline{k}_{0s}, g_1, g_2, \overline{H}^1, \overline{H}^1_y)$.

III. For $j = 2, 3, \ldots, n$ solve the overdetermined system (3.12) by the normal equations method, giving

$$B^*\left(\beta_j - \frac{\Delta\omega}{2}\right)B\left(\beta_j - \frac{\Delta\omega}{2}\right)\overline{p}^j = B^*\left(\beta_j - \frac{\Delta\omega}{2}\right)S^{p,j}(\beta_j, \Delta\omega, \overline{k}_{0s}, g_1, g_2, \overline{p}^1, \overline{p}^2, \ldots, \overline{p}^{j-1}, \overline{H}^1, \overline{H}^1_y). \tag{3.13}$$

IV. Evaluate

$$\overline{H}^n \approx \Delta\omega\left[-\frac{\overline{p}(\omega_n)}{2} - \sum_{l=2}^{n-1}\overline{p}(\omega_l) - \frac{\overline{p}(\omega_1)}{2}\right] + \overline{H}^1.$$

V. Evaluate $\overline{H}^n_y$ from $\overline{H}^n$ using FD.

VI. Use (3.2) at $\omega = \omega_{\min}$ to compute the updated value for $\overline{h}$, using $\overline{H}^n$ and $\overline{H}^n_y$.

4. An effective preconditioner for the conjugate gradient method

The marching technique of the previous section required the solution of an overdetermined system of the form $B^j\overline{x}^j = \overline{b}^j$, $j = 1, 2, \ldots, n$, where $\overline{x}^j$ was either $\overline{H}^j$ or $\overline{p}^j$ and B^j was $B(\omega_j)$ or $B(\omega_j - (\Delta\omega/2))$. We have chosen to use the normal equations method, which leads to solving $B^{j*}B^j\overline{x}^j = B^j\overline{b}^j$, $j = 1, 2, \ldots, n$. Since B^j is essentially a banded matrix similar to that resulting from the Laplacian operator, $B^{j*}B^j$ is a 13-band matrix which can be explicitly evaluated at little cost. Denote $B^{j*}B^j$ by A^j. Since the columns of B^j are linearly independent, A^j is clearly invertible, and hence Hermitian Positive Definite (HPD). In contrast, for integral equation-based methods, a full matrix system has to be solved. This limits the number of grid points which can be used. But even in the case of a band matrix, conventional Cholesky factorization techniques are needlessly time consuming, so iterative algorithms are to be preferred. In the case of a HPD matrix the preconditioned conjugate gradient method is a natural choice. But the key issue as usual is the selection of a preconditioner.

4.1. Direct methods

We will begin by considering direct sparse factorization methods for HPD matrices. The three most common highly efficient direct techniques for the case where fast Fourier transform methods are not available are skyline, one way dissection (1WD) and nested dissection (ND) [12]. Each approach requires reordering the unknowns, and hence permuting the rows and columns of A^j. Thus the actual system to be solved instead of $A^j\overline{x}^j = \overline{b}^j$ is $PA^jP^*\overline{y} = P\overline{b}^j$, where $\overline{y} = P\overline{x}^j$, and P is a permutation matrix. For a rectangular region such as is present for this problem, the skyline method tends to reorder unknowns along the shorter side; the one way dissection method places separators along the grid, giving a series of decoupled problems which are then joined on the bottom rows of the new matrix; and nested dissection uses separators in both directions. For square grids of size m by m and Laplacian type operators these factorization methods are of order $\mathrm{O}(m^4), \mathrm{O}(m^{3.5})$ and $\mathrm{O}(m^3)$, respectively [12]. The corresponding storage sizes are of order $\mathrm{O}(m^3), \mathrm{O}(m^{2.5})$ and $\mathrm{O}(m^2 \ln m)$. As is not so well known, these asymptotic rates often require rather large values of m to be relevant. Thus in practice there are various crossover points, below which, for example, skyline methods are best.

A 201×71 size grid giving a matrix of size 14,271 will typically be used, and for comparison a 301×106 grid with a 31,906 size matrix will also be considered. The efficiency of the solve part will later prove to be very important when many solves will be calculated for each factorization using the preconditioned conjugate gradient method. Efficient storage is also an issue. In their classic text, George and Liu [12] develop and implement all the above methods, including orderings, storage structures, factorizations, and solves. However their implementations were for real valued positive definite systems, not Hermitian ones. For this reason it was necessary to modify their various routines to generalize them to Hermitian matrices. This primarily involved switching to complex arithmetic and paying careful attention to where conjugates must be used. This procedure has been carried out for all of the three above methods. It should be noted that improved implementations, for example for the factorization and solves, have been recently developed that better use cache memory by concentrating more of the work on small dense matrices or by the use of frontal methods [8,11], but little of this is currently within the public domain [8]. The preconditioning approach developed in the next section would immediately apply to any such improved methods.

In Table 2 below results are presented of applying these three methods to the two matrix systems considered above, for factorization and solve times, plus storage. It should be noted that the actual run times for the different methods are in general not proportional to the operation counts since the simpler methods such as skyline tend to achieve a higher efficiency. There are of course also memory cache issues. The implementations below are computed on a SGI Origin 200 using one processor and (mostly) double precision complex arithmetic. Times are in seconds and storage is in megawords. Each megaword requires

Table 2
A comparison of factor and solve times, and storage for three different direct sparse methods applied to two different matrices

Matrix size	ND			1WD			Skyline		
	Factor	Solve	Storage	Factor	Solve	Storage	Factor	Solve	Storage
14,271	2.88	.099	.855	4.99	.113	.503	4.56	.265	1.769
31,906	10.64	.254	2.212	21.4	.32	1.399	22.23	.875	5.929

8–16 megabytes (MB) of storage. All factorizations and conjugate gradient calculations are computed in double precision, but the factored complex matrix is stored and used only in single precision. This is primarily for efficiency, as the memory communication is somewhat faster using single precision, and the truncated preconditioner is about as effective as its original double precision version. This also proves advantageous for purposes of minimizing memory when the possibility of reusing the preconditioners in multiple sweeps is considered, but this was not the primary motivation.

As can be seen the ND method has by far the fastest factorization times, with the faster asymptotic factorization times of 1WD as compared to the skyline method only dominating for the larger matrix, and then only marginally. The solve times, which will dominate the PCG calculations, are somewhat better for ND than 1WD, but far better than for skyline for both matrices. For both matrix sizes, 1WD has the smallest storage, with the skyline method having far greater storage requirements. If storage were the critical issue, 1WD would be the preferred method, with ND being only about 12% faster for the solves and 42% faster for the factorizations. The effective time required for 1WD versus ND in the context of the PCG method for the smaller matrix will be reported later. Since storage for ND is a modest 14–36 MB in double precision plus other overhead, this method will be focused on as the method of choice, given its superior factorization and solve times compared with the other two direct sparse methods.

4.2. A preconditioned conjugate gradient method

As might be expected, the above sparse direct results can be significantly improved by use of the PCG method [13,22] with the key question involving, as usual, the choice of an effective preconditioner. It is common when applying the conjugate gradient method to the normal equations to form the matrix vector product not as $(B^{j*}B^{j})\bar{x}$ but instead as $B^{j*}(B^{j}\bar{x})$, so as to perform just two matrix vector products instead of the often more expensive matrix product [22]. Due to the simple band structure of B^{j}, the matrix matrix multiply is inexpensive in our case, and there is an advantage to having just one matrix A^{j} in explicit form. The issue of finding an effective preconditioner here is especially pressing since the convergence rate of the conjugate gradient method [13] is $(\sqrt{k}-1)/(\sqrt{k}+1)$ or approximately $1-2/\sqrt{k}$, where k is the condition number of A^{j}, and the condition number of A^{j} is the square of the ratio of the largest to the smallest singular values of the original matrix B^{j} Saad [22] comments that "Recent research on iterative techniques has been devoted in great part to the development of better iterative accelerators, while 'robust' preconditioners have by and large been neglected". He also comments that "normal equations are also difficult to precondition". It is the development of such a robust preconditioner for this family of normal equations that is the focus of this section.

Here a sequence of problems must be solved where the matrix depends only on the frequency ω and hence can be evaluated at any time. For both methods each right-hand side can only be computed after the successful solution of the previous system. But since the matrix $B^{j}=B^{j}(\omega_{j})$, for frequency ω_{j}, changes only slowly for nearby frequencies, its factorization leads to an approximate inverse for *many* nearby frequencies. Moreover this method is a general method applying not only to both cases under consideration here, but also to any situation involving the system $A^{\omega}x^{\omega}=b^{\omega}$ where many right-hand sides b^{ω} must be solved for a family of matrices A^{ω}, that change slowly with respect to ω. Even if the matrices A^{ω} were not HPD, iterative methods other than conjugate gradient such as GMRES [21] could be used, with one factorization of A^{ω} serving as the preconditioner. It is the fact that the factorization cost can be amortized over conjugate gradient solutions for many right-hand sides that makes this approach attractive. Moreover, the preconditioner can be evaluated in a centered position over the next set of frequencies, so that it is effective for both earlier and later frequencies inside the set.

This approach will be combined with the observation that the solution vector also systematically changes with ω, allowing for extrapolation methods to be used. It has been found that a fourth order method (cubic fit) works well, and decreases the number of iterations, by giving a better starting value. Using this approach usually 1–15 iterations are all that are required to reduce the residual by six orders of magnitude. An automatic algorithm has been developed to give a dynamic mix of the number and placement of symmetrically placed preconditioners for matrices related to the set of frequencies $[\omega_{\min}, \omega_{\max}]$ with a separation $\Delta\omega$. This algorithm is robust over changes in the CPU, operating system, selection of the sparse matrix direct factorization and solve methods, cache usage, the frequency density $\Delta\omega$, and the upper and lower frequencies used, etc. It locally varies the placement of the next preconditioner matrix to be evaluated, and has a criterion for when to start the next series of frequencies. A new preconditioner is evaluated when the current PCG solve time becomes greater than the average weighted total solution time (one factorization at a half weight and many PCG solves for frequencies ω_j at or below the frequency ω_{Center} where the preconditioner is factored). The algorithm, in a simplified form, is presented below in pseudocode. Recall that the frequencies are decreasing.

```
$\Delta\omega 2 = \{0$ for the $H$ method, $\Delta\omega/2$ for the $p$ method$\}$
Restart = .True.; $jcenter = 1$;
For $j = 1 : n$
    If (Restart); Use ND to compute the factorization of $B^*(\omega)B(\omega)$ at $\omega = \omega_{jcenter} - \Delta\omega 2$ in time $TFactor$; $Tcum = TFactor/2$; $Ncount = -1/2$; Restart = .False.
    Setup the next problem at $\omega = \omega_j - \Delta\omega 2$, using a cubic extrapolation from the previous solutions as a starting value for the PCG method.
    Call a PCG routine with the above factorized matrix as a preconditioner to solve (3.3) or (3.13) in time $Tsol$.
        $Tcum = Tcum + Tsol$; $Ncount = Ncount + 1$;
        If $(Tsol > Tcum/Ncount)$; $jcenter = j + (j - jcenter)$ ; Restart = .True.
End
```

To summarize, in this algorithm the key choices are when to compute a new preconditioner, and how far ahead it should be placed. How far ahead to place it is selected based on the number of successful steps since the last preconditioner was evaluated. The use of the half weight is to also amortize *TFactor* over the frequencies above $\omega_{jcenter}$ which implicitly have weights of zero. No use is made of the time to progress to the next $\omega_{jcenter}$, although as a rule the intervals are nearly symmetric.

4.3. Performance tests

The performance of this preconditioner approach will be measured in two ways: by varying the frequency spacings and by varying the underlying spatial mesh density. Spatial meshes of 201 × 71 and 301 × 106, frequency densities of .01, .02, .05, and .10 GHz over an overall frequency range .52–3.0 GHz with fourth order extrapolations from the previous solutions to the next solution and the ND method will be used. In addition solutions over the 201 × 71 mesh using 1WD $(*)$ in place of ND, and also with ND but no extrapolation $(\dagger)$ will be evaluated. Zero will be used for the starting iterate at the first frequency, and iterations will stop when the residual is six orders of magnitude smaller than the initial right-hand side in the $\mathscr{L}^2$ norm. Results are reported for both the p- and H-methods.

The reportage in 3 gives five results for each run: The total number of preconditioners used; the average number of iterations until convergence; the maximum number of iterations; the total time (bold); and the average time per setup and solution for each matrix system, including the preconditioner times.

4.3.1. Extrapolation of solutions

Comparing the second and third rows of Table 3 for both the p- and H-methods for average times shows that the extrapolation approach for starting iterates is very successful for the two denser frequency sets .01

Table 3
Single sweeps with four frequency densities, two spatial meshes

p-Method	.01 GHz (248 freq.)	.02 GHz (124 freq.)	.05 GHz (49 freq.)	.10 GHz (24 freq.)
$201 \times 71^{*}$	12, 3.6, 6, **240**, 0.97	10, 5.3, 10, **171**, 1.38	7, 7.2, 15, **98**, 1.99	5, 10.8, 27, **69**, 2.88
$201 \times 71^{\dagger}$	20, 5.0, 8, **256**, 1.03	16, 5.4, 9, **154**, 1.24	9, 7.1, 14, **80**, 1.63	6, 9.4, 18, **51**, 2.14
201×71	15, 3.3, 5, **193**, 0.78	12, 4.8, 9, **134**, 1.08	9, 6.0, 11, **74**, 1.51	6, 9.4, 18, **52**, 2.17
301×106	13, 3.4, 6, **513**, 2.07	10, 5.1, 10, **368**, 2.96	7, 6.9, 14, **209**, 4.26	5, 10.4, 25, **147**, 6.10
H-Method	.01 GHz	.02 GHz	.05 GHz	.10 GHz
$201 \times 71^{*}$	10, 2.6, 5, **191**, 0.77	9, 4.3, 9, **148**, 1.19	7, 6.8, 14, **94**, 1.93	5, 10.8, 32, **69**, 2.89
$201 \times 71^{\dagger}$	22, 5.0, 8, **263**, 1.06	16, 5.6, 10, **156**, 1.26	9, 7.4, 15, **82**, 1.67	7, 8.7, 16, **52**, 2.19
201×71	11, 2.5, 5, **155**, 0.63	10, 3.9, 8, **114**, 0.92	8, 6.0, 11, **71**, 1.45	6, 9.1, 20, **51**, 2.13
301×106	9, 2.6, 5, **403**, 1.63	8, 4.1, 7, **303**, 2.44	6, 7.0, 17, **199**, 4.07	5, 10.8, 25, **150**, 6.26

and .02 GHz, and is especially advantageous for the H-method, and successful to a lessor degree for the frequency spacing of .05 GHz. It has little impact at .10 GHz.

4.3.2. Comparing 1WD with ND

Comparing the third and fourth rows, the use of 1WD instead of ND increases the run time for a single sweep by about one third. For multiple sweeps the preconditioner factorizations could be held in RAM, further minimizing the effect of the factorization costs. If RAM were limited, for example to 128 MB on a PC, the use of 1WD, with multiple sweeps and preconditioner recall, would give a final throughput dominated by the solve times. From Table 2, the additional memory usage would be about 4 MB per preconditioner. Of course where sufficient RAM is available, ND is the method of choice, but for multiple sweeps and recall, the relative timing advantage would not be great compared with the gain achieved by reuse of the preconditioners. The use of 1WD will not be explored further here.

4.3.3. Scalability of the ND approach with extrapolation

For the ND runs the convergence rate seems fairly independent of these matrix sizes, as the algorithm automatically shifts towards fewer preconditioners, and slightly more iterations to compensate for the longer factorization times. The method seems to be exhibiting excellent scalability for ND, with the total solution times increasing by factors from about 2.6 to 2.9 as the matrix size increases by a factor of 2.2.

5. Numerical experiments

The main goal of the numerical experiments presented in this section is to consider and compare the properties and performance of the proposed algorithms for realistic ranges of parameters and frequencies. The values of the coefficients in the Helmholtz equation, which correspond to the electromagnetic properties of air, soil, and different targets were presented in Table 1. In the numerical experiments the background medium consists of air and wet soil with a 5% moisture content. The targets are assumed to be filled with TNT.

The physical domain for the inverse problem is selected to be $[-L_x, L_x] \times [0, L_y]$, where $L_x = 60\,\text{cm}$ and $L_y = 40\,\text{cm}$, with a 201×71 grid. Other grid and frequency selections would be chosen for other applications. In both approaches the system was nondimensionalized in space and frequency. However for simplicity the results are presented here in the original coordinate systems. The spatial grids selected are uniform, but do not necessarily have the same spacings in x and y.

5.1. A single inclusion of circular shape filled with TNT

To demonstrate the robustness of this technique, consider a circular target filled with TNT, with center at $\mathbf{x} = (x_0, y_0) = (10, 5)$ cm and a diameter of 5 cm. Thus $h(\mathbf{x}) = (k_{\mathrm{TNT}}^2 - k_{\mathrm{wetsoil}}^2)/k_{\mathrm{wetsoil}}^2 = -0.319 - 0.152\mathrm{i}$. The real part of the corresponding function $h(\mathbf{x})$ is displayed in Fig. 1.

5.2. Noise removal by cubic splines in the forward solution

For this application simulations are made using the forward solution for the discrete frequencies $\omega = 2\pi \times [.50 : .01 : 3.00]$ GHz. The physical domain is taken to be a square with 300 cm sides centered about the air–soil interface, and a 400×400 point computational grid is used to achieve accuracy at the higher frequency values. In the inverse problem $\omega_{\min}$ and $\omega_{\max}$ are chosen so that $2\pi \times .50\,\mathrm{GHz} \leqslant \omega_{\min} < \omega_{\max} \leqslant 2\pi \times 3.00\,\mathrm{GHz}$, and the frequency spacing is taken to be uniform from $\omega_{\min}$ to $\omega_{\max}$, but this is not a requirement of the method. Two of the studies to be made here consider the effect of various choices of $\omega_{\min}, \omega_{\max}$ and the frequency spacing $\Delta\omega$ on the quality of the inverse problem solution.

For Figs. 2–4 the solid line represents the real parts of the original values obtained through the solution of the forward problem, the stars, which are the data originally received by the algorithm, represent those values with $\sigma = .10$ multiplicative Gaussian noise added and the dot-dash line the result after the spline smoothing process described in Section 3. Figs. 2 and 3 display the real parts of $H(\mathbf{x}, \omega) = \widetilde{\varphi}(10, \omega)$ and the normal derivative $H_y(\mathbf{x}, \omega) = \widetilde{\psi}(10, \omega)$ as a function of $f = \omega/2\pi$, just above the target at $\mathbf{x} = (10, 0)$ on the air–soil interface. Despite the scatter in the noisy data, the C^2 cubic spline smoothing process appears to be doing a good job of returning smoothed values close to the original. The largest differences are around the peaks of the curves and to the far left of Fig. 3. Fig. 4 displays the real part of $H(\mathbf{x}, \omega_0) = \widetilde{\varphi}(x, \omega_0)$ along the air–soil interface ($y = 0$) for $\omega_0 = 1.0 \cdot 2\pi$ GHz. It should be clarified, that smoothing was done for each spatial point $\mathbf{x} = (x_i, 0)$, where $x_i = -L_x + \Delta x(i - 1/2),\ i = 1, \ldots, M_x$, with respect to the frequency ω as described above. However, no smoothing was performed with respect to the spatial variable $\mathbf{x}$.

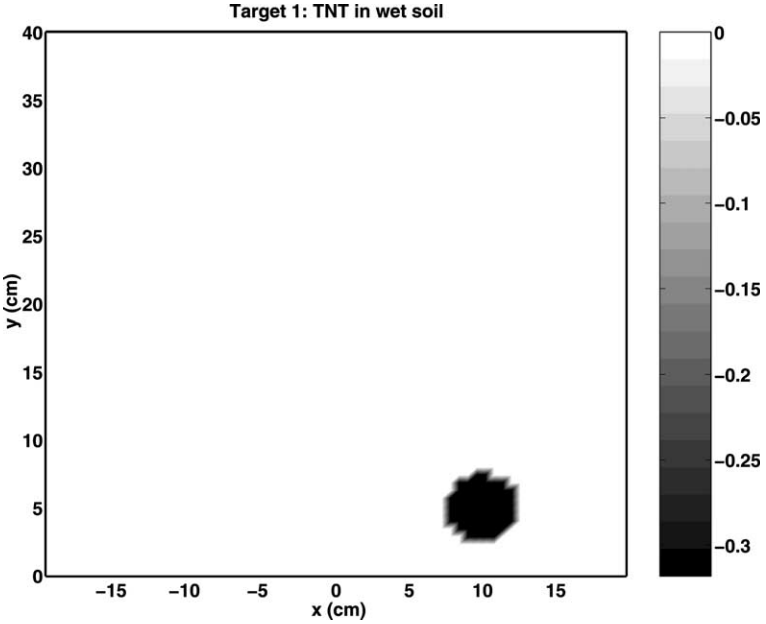

Fig. 1. Re$[h(\mathbf{x})]$ for a circular shaped target filled with TNT.

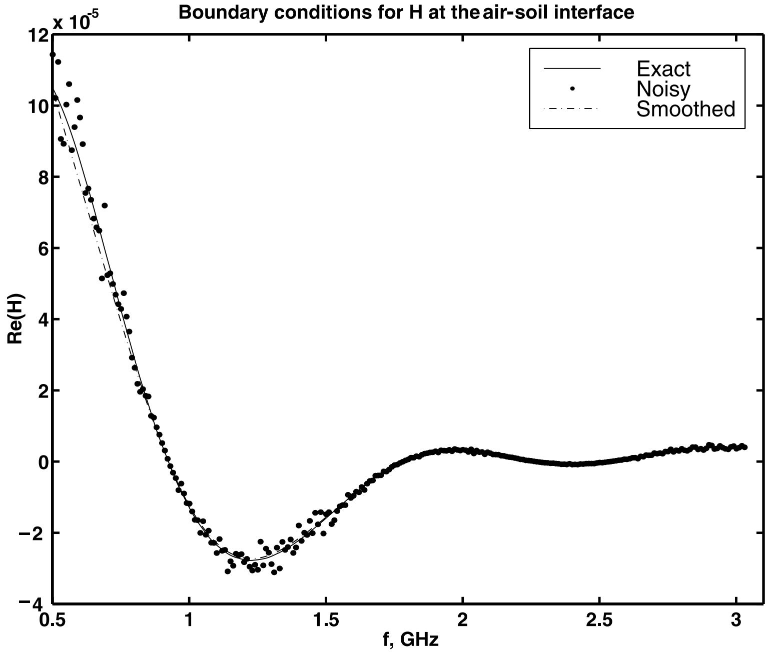

Fig. 2. Re$[H(\mathbf{x}, \omega)]$ as a function of the frequency f at $\mathbf{x} = (10, 0)$.

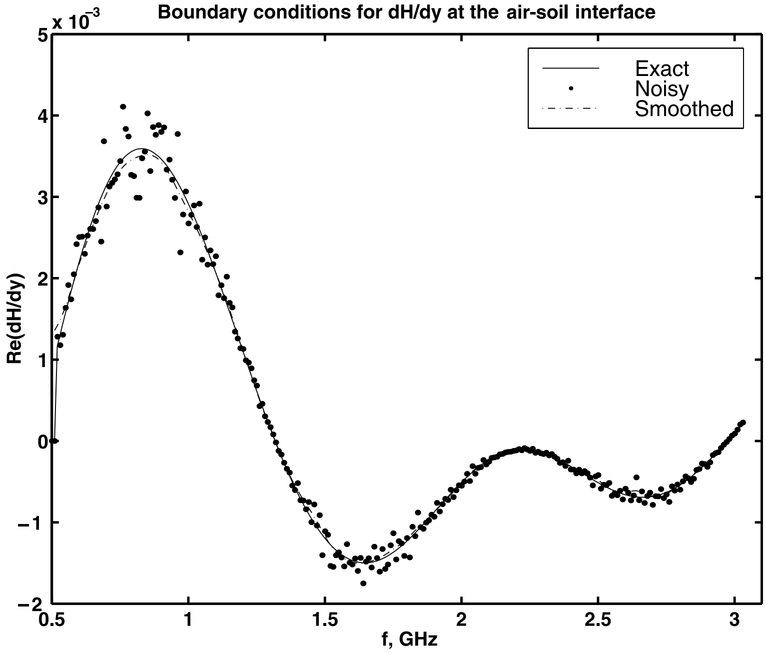

Fig. 3. Re$[H_y(\mathbf{x}, \omega)]$ as a function of the frequency f at $\mathbf{x} = (10, 0)$.

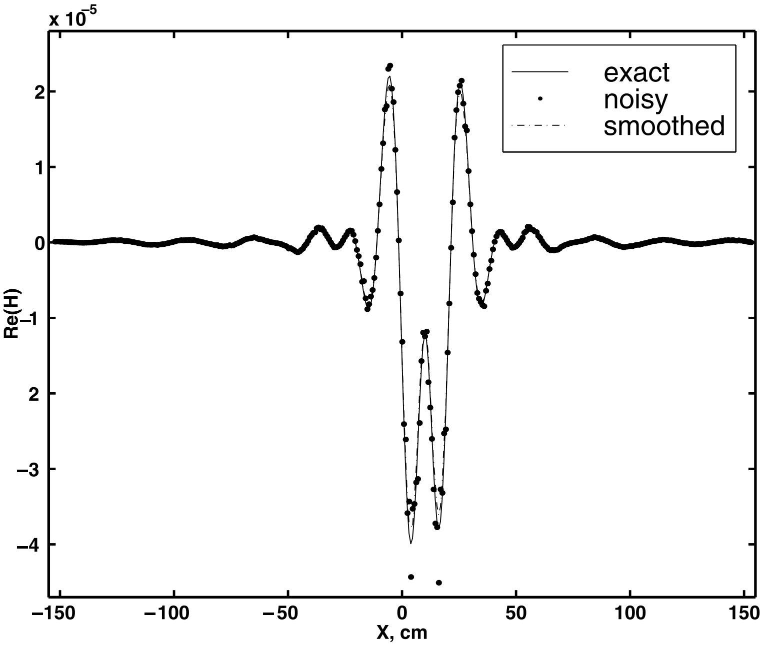

Fig. 4. $\mathrm{Re}[H(x,\omega_0)]$ for $\omega_0 = 1.0 \cdot 2\pi$ GHz as a function of x along $\{y = 0\}$.

5.3. Single target solutions by the H- and p-methods

In this first test the H- and p-imaging algorithms were applied to a single target of circular shape filled with TNT as specified in Section 5.1. The results used data over frequencies from .5 to 3 GHz, using an increment of $\Delta f = .01$ GHz. Figs. 5 and 6 display the real part of the imaged function $h := h_{\mathrm{imaged}}(x, y)$ obtained after one sweep of the H-method and two sweeps of the p-method, respectively. The contour plots of the recovered function Real(h) are similar, both accurate as to the centered location, both lacking significant artifacts, except that the H-solution is slightly lower in its recovered coefficient values. The vertical image size and lack of diagonal artifacts are somewhat more favorable for the H-method. The imaginary part of h here and elsewhere is in general less satisfactory, which is related to problems in phase recovery.

The stopping criteria here and elsewhere requires running one more sweep than was used, stopping when the last result either decreased, showed significant oscillations or changed very little. The value of k for the inner iterations of the H-method was always selected to be $k = 1$.

5.4. The effect of the upper frequency cutoff ω_{max} on solutions

In this subsection the effects of using frequencies from $f_{\mathrm{min}} = .50$ GHz to various upper values of $f_{\mathrm{max}} = \omega_{\mathrm{max}}/2\pi$ from 1.0 to 3.0 GHz is considered for both the H- and p-methods. The frequency spacing Δf is fixed at .01 GHz. To clearly demonstrate the results quantitatively, cross-sections of the real part of the imaged function h along both vertical and horizontal lines are displayed for each method. In each case, the cross-section is along the line where the values are greatest. Typically for the horizontal lines this is close to $y = 5$ cm, and for the vertical lines close to $x = 10$ cm. In Figs. 7–10 the solid lines represent the exact values and various other lines, as identified by the legend, the cross-sections of various computed solutions.

As one can see increasing of the range of the frequencies from 0.5–1 to 0.5–1.5 to 0.5–2 GHz gives significant improvements in the heights of the recovered images for both the H- and p-methods and is

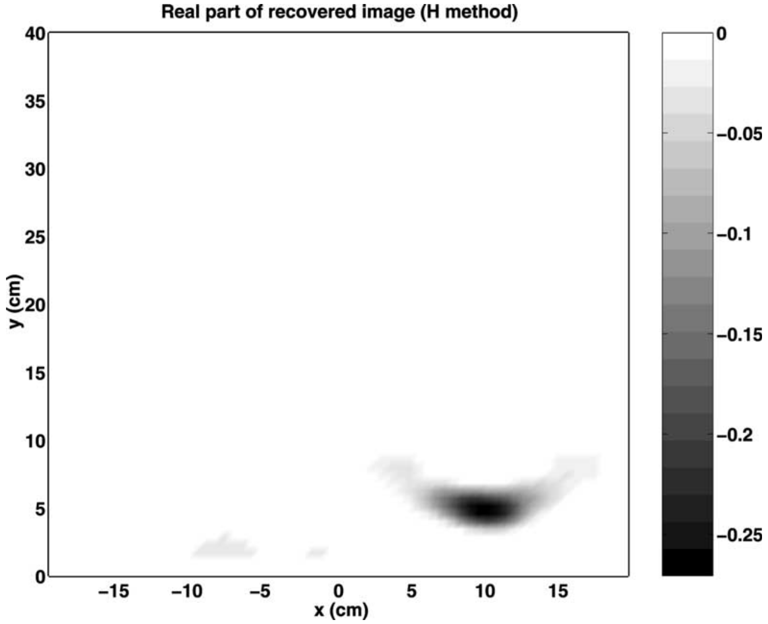

Fig. 5. $\mathrm{Re}[h_{\mathrm{imaged}}(\mathbf{x})]$ for the solution of the inverse problem by the H-method.

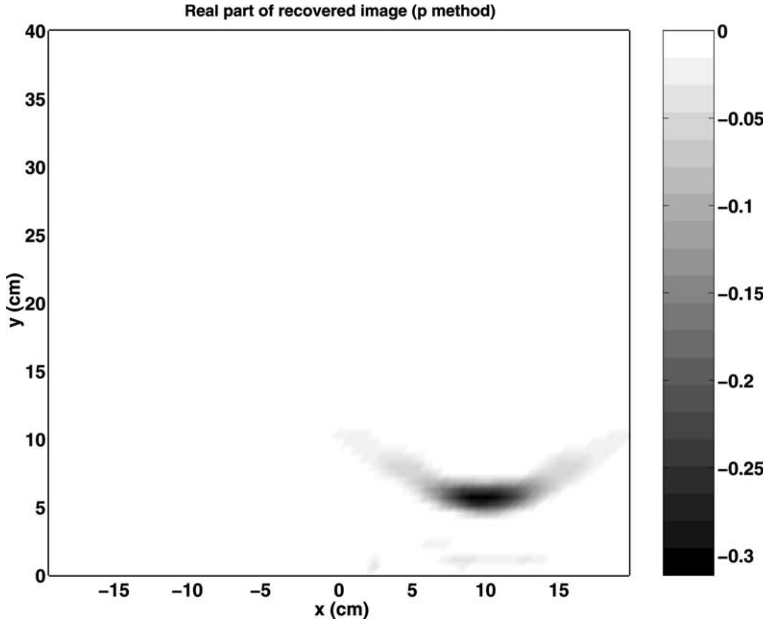

Fig. 6. $\mathrm{Re}[h_{\mathrm{imaged}}(\mathbf{x})]$ for the solution of the inverse problem by the p-method.

thus clearly desirable. The effect of increasing the upper limit to 2.5 or 3 GHz is more complicated. In Figs. 7 and 9, the H-method with horizontal and vertical cross-sections, there appears to be no advantage to going beyond $f_{\max} = 2\,\mathrm{GHz}$. This is a favorable conclusion for the H-method both from

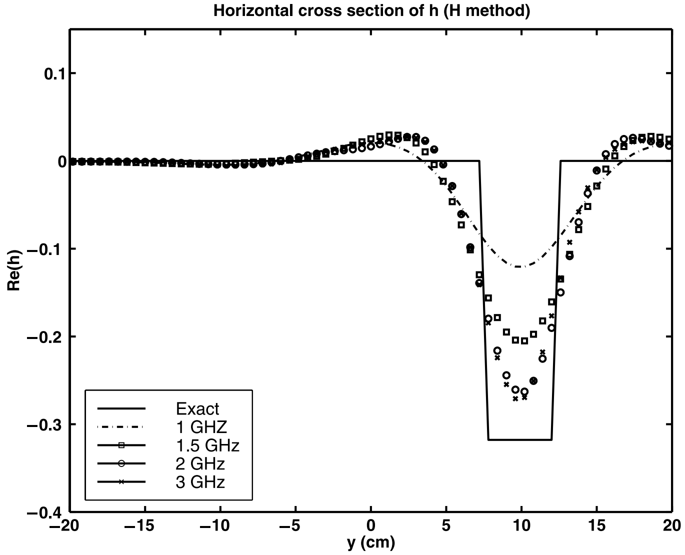

Fig. 7. Horizontal cross-sections of $\mathrm{Re}[h_{\mathrm{imaged}}(\mathbf{x})]$ after one sweep using the H-method for different values of $\omega_{\max}$.

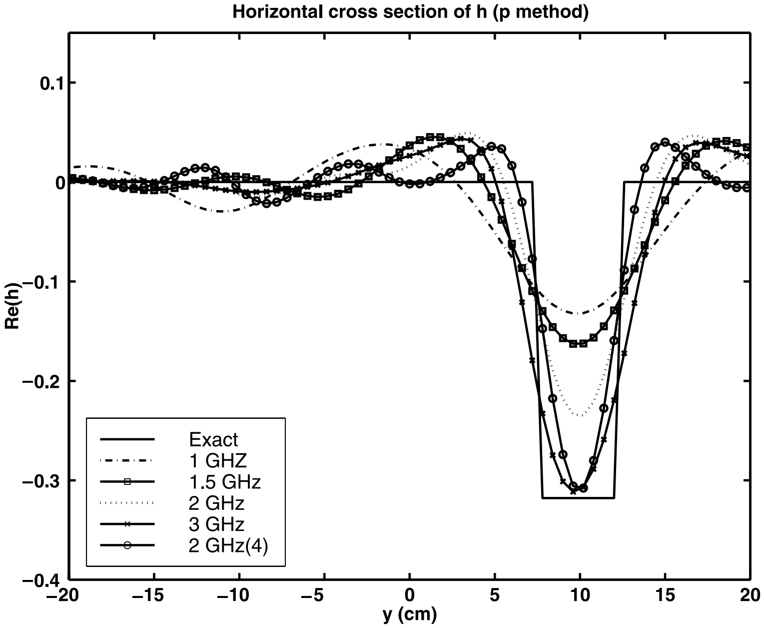

Fig. 8. Horizontal cross-sections of $\mathrm{Re}[h_{\mathrm{imaged}}(\mathbf{x})]$ after two sweeps using the p-method for different values of $\omega_{\max}$.

the viewpoint of the significantly reduced physical measurement requirements and reduced computational requirements. Also all results were achieved in the first sweep, using the stopping criteria of the previous subsection. In Figs. 8 and 10, the p-method, all results were achieved after two sweeps. Since using the frequency range 0.5–3 GHz gives slightly improved values over 0.5–2.5 GHz, $f_{\max} = 3$ GHz

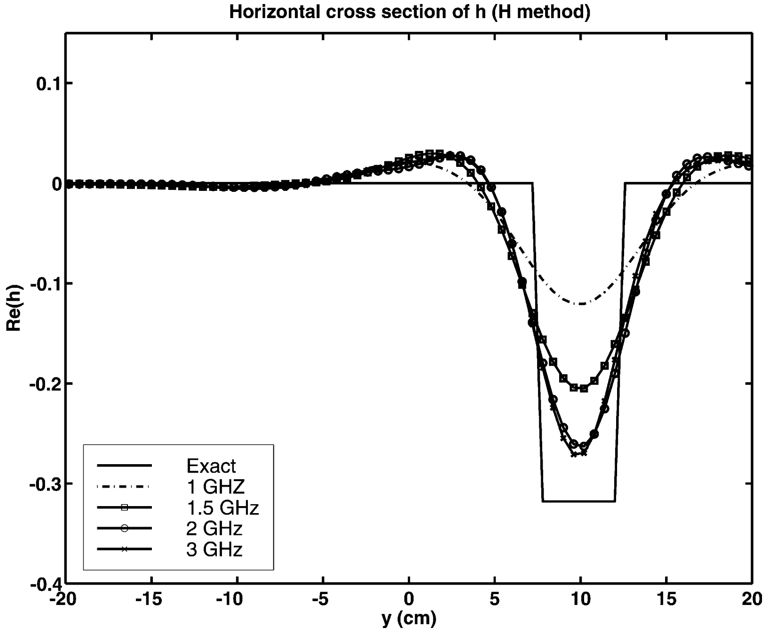

Fig. 9. Vertical cross-sections of $\mathrm{Re}[h_{\mathrm{imaged}}(\mathbf{x})]$ after one sweep using the H-method for different values of $\omega_{\max}$.

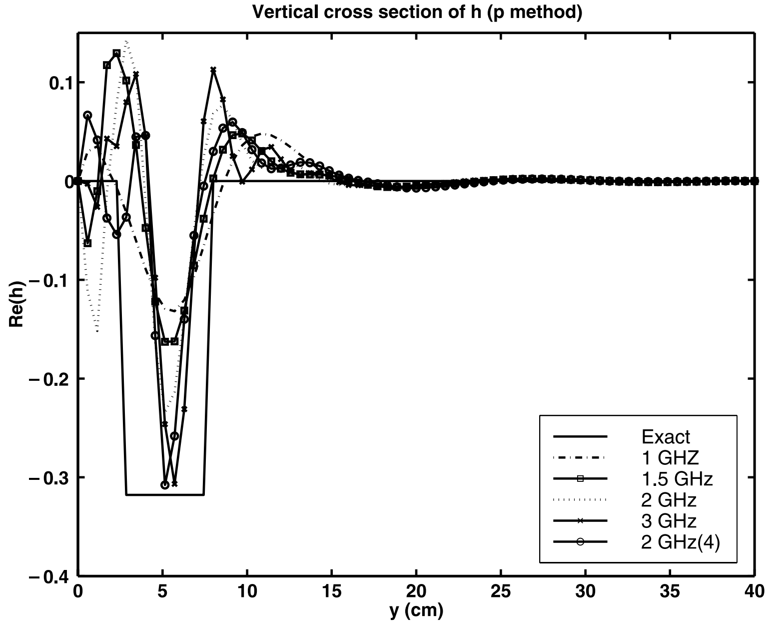

Fig. 10. Vertical cross-sections of $\mathrm{Re}[h_{\mathrm{imaged}}(\mathbf{x})]$ after two sweeps using the p-method for different values of $\omega_{\max}$.

will be used for the p-method in the remainder of this paper, although the alternative choice of $f_{\max} = 2.5\,\mathrm{GHz}$ could give similar results. The accurate horizontal width of the target originally seen in Figs. 5 and 6 can also be observed in Figs. 7 and 8. The insufficiently sized vertical target widths

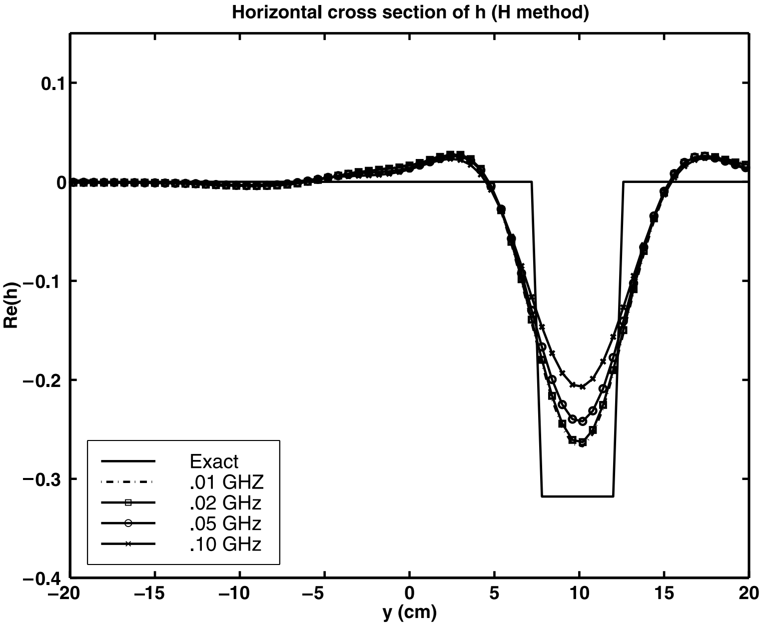

Fig. 11. Horizontal cross-sections of $\mathrm{Re}[h_{\mathrm{imaged}}(\mathbf{x})]$ after one sweep using the H-method for different values of $\Delta\omega$.

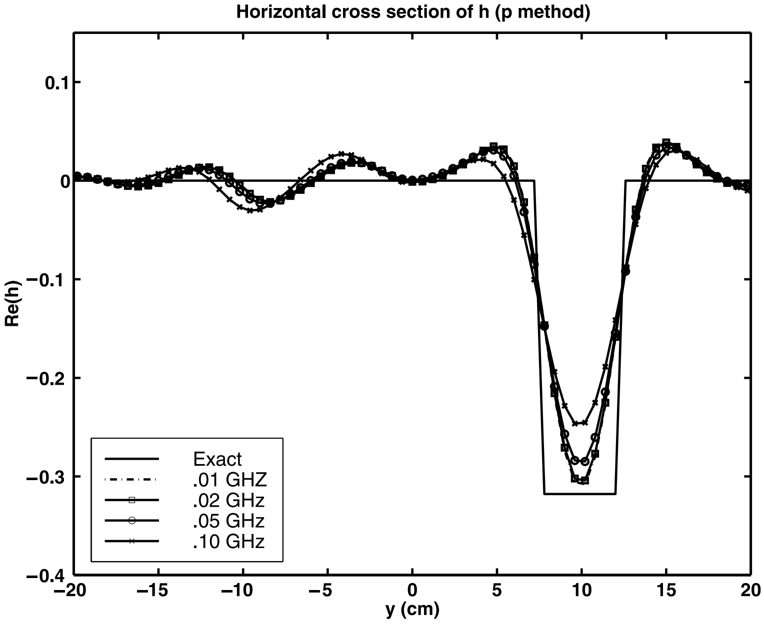

Fig. 12. Horizontal cross-sections of $\mathrm{Re}[h_{\mathrm{imaged}}(\mathbf{x})]$ after two sweeps using the p-method for different values of $\Delta\omega$.

generated by both methods can be observed in Figs. 9 and 10, which also show clearly the higher quality of the size of the vertical width given by the H-method, which was earlier observed in Figs. 5 and 6.

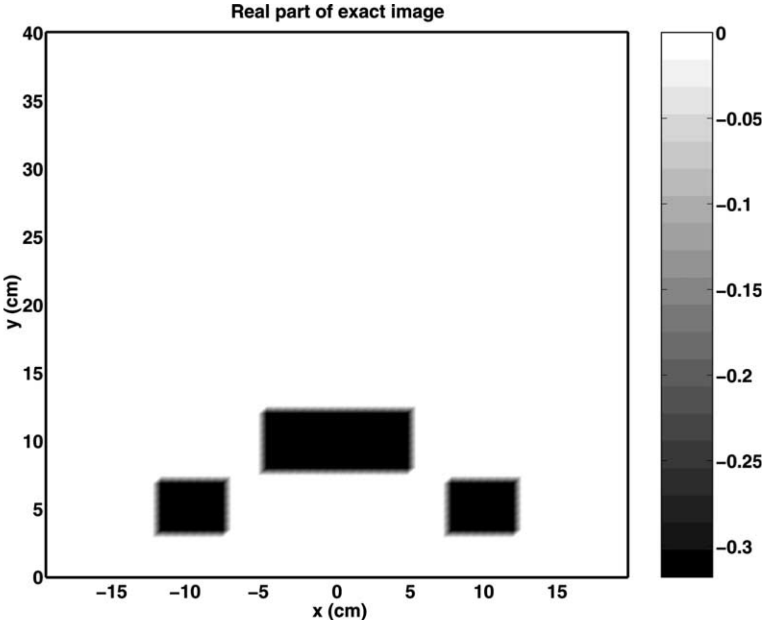

Fig. 13. Re[$h(\mathbf{x})$] for multiple mine-like targets of various sizes.

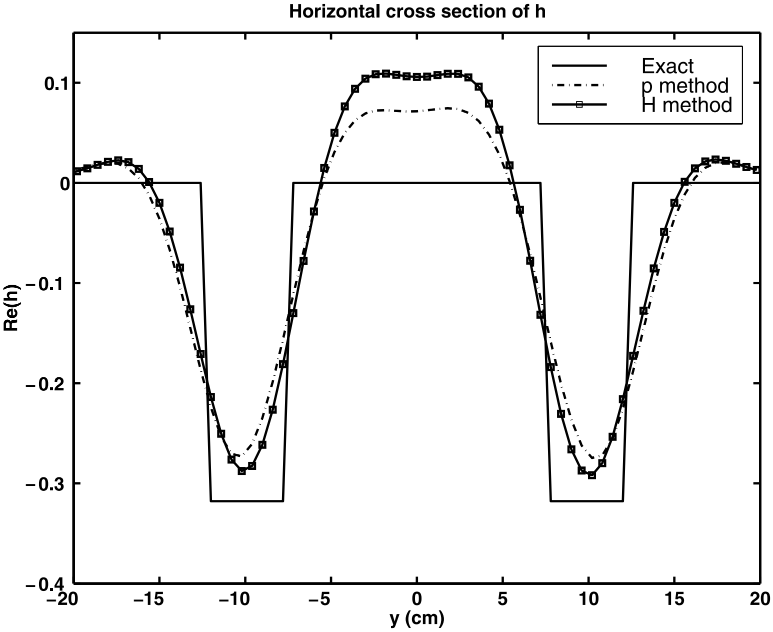

Fig. 14. Horizontal cross-sections of Re[$h_{\text{imaged}}(\mathbf{x})$] using the H- and p-methods.

5.5. *The effect of the frequency density $\Delta\omega$ on solutions*

In this subsection the effect of various frequency spacings $\Delta f = \Delta\omega/2\pi$ will be examined, where $f_{\max}$ is fixed at 2 GHz for the H-method and 3 GHz for the p-method. Runs for $\Delta f = .01$, .02, .05, and .10 GHz are considered for both the H- and p-methods. All H-method runs stopped after one sweep, and all p-method runs after 2 sweeps. As usual, one additional sweep was required to determine that the stopping criteria was satisfied. Figs. 11–14 show that at a frequency step of $\Delta f = .10$ GHz the results were too low, but increasing as Δf decreased. The results for $\Delta f = .02$ and .01 GHz were almost coincident, and are difficult to distinguish on the figures. The conclusion is clear: it is unnecessary to use such a fine computational frequency density as $\Delta f = .01$ GHz; results of a comparable quality are achieved by use of the coarser frequency density of $\Delta f = .02$ GHz.

5.6. Multiple targets filled with TNT

In the remaining numerical examples the application of the two algorithms to the case of multiple mine-like targets of different sizes and soil depths is considered. These targets are again in wet soil and filled with TNT, using parameter values from Table 1. The buried objects chosen for this test are three rectangular mine-like targets. Two of the targets are 5×4 cm and the third is 10×4 cm. Three mine-like targets were examined to see if the H- and p-inversion algorithms could separate multiple scatterers and reconstruct well the deeper object. The frequency range in this test is from 0.5 to 2.0 GHz for the H-method and 0.5 to 3 GHz for the p-method, and the frequency step is $\Delta f = 0.02$ GHz as suggested by the previous subsections. The two smaller targets are centered 5 cm into the ground and the larger rectangular target is centered 10 cm deep into the ground. The horizontal centers are at -10, 0, and 10 cm. As in the first example, the detector readings are simulated from the forward problem with the addition of $\sigma = .10$ multiplicative Gaussian noise.

The real part of the corresponding function $h(\mathbf{x})$ is displayed in Fig. 13. Using the H- and p-methods, the reconstructed images of the real part of the coefficient are shown in Figs. 15 and 16. From these figures it can be seen that both algorithms perform reasonably well. The locations and shapes of the objects are both

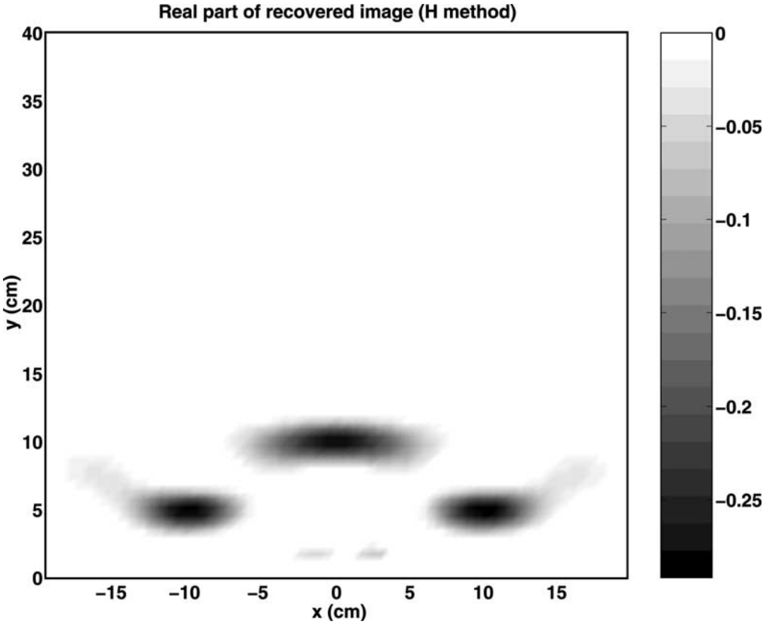

Fig. 15. Final reconstruction of $\mathrm{Re}[h_{\text{imaged}}(\mathbf{x})]$ after one sweep using the H-method.

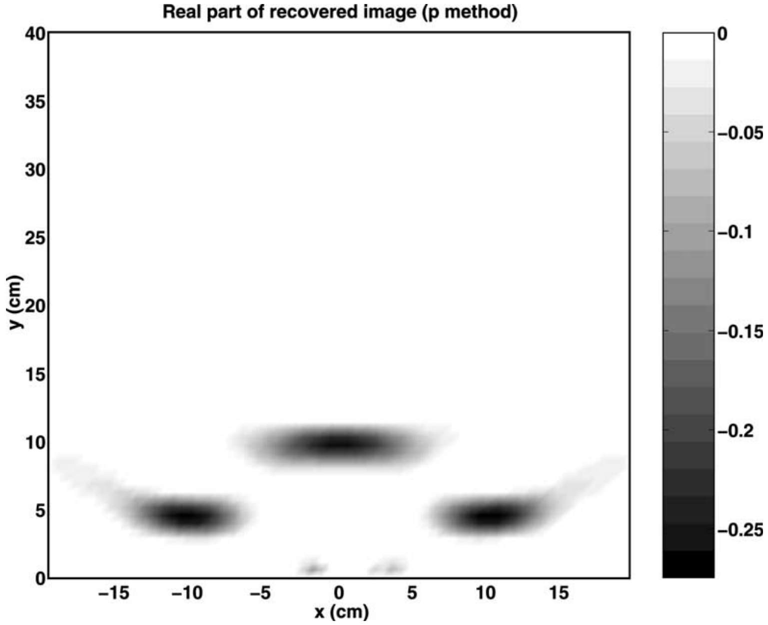

Fig. 16. Final reconstruction of $\mathrm{Re}[h_{\mathrm{imaged}}(\mathbf{x})]$ after one sweep using the p-method.

fairly accurate, with the results from the H-method being marginally better in value and notably better for centered vertical locations and sizes. In Fig. 14, in order to provide a more quantitative comparison, the cross-section of the real part of the image along the horizontal line where it is greatest in value (about $y = 5$ cm for the H-method, closer to $y = 4$ cm for the p-method) is presented for both methods. Both methods stopped after one sweep. The total time for the H run (two sweeps) shown in Fig. 15 was 147 and 301 s for the p run shown in Fig. 16 also at two sweeps (the second sweeps were required to satisfy the stopping criteria).

5.7. Numerical conclusions

In the above numerical experiments both methods gave similar results using an upper bound for frequency of 2.0 GHz for the H-method and 3 GHz for the p-method, and a Δf of 0.02 GHz. For both examples the horizontal widths and locations of the recovered images were rather accurate, while the H-method was in general better for vertical widths and locations. For the single target example, the p-method showed a final image that at its extreme centered real value was somewhat closer to the target value than the H-method. However (not counting the termination sweep) the H-methods required only one sweep with an upper bound of 2.0 GHz, while the p-method required 2 sweeps in the single target case and one sweep in the multiple target case and with an upper bound of 2.5–3.0 GHz for $f_{\max}$. This increased upper bound for $f_{\max}$ not only notably increases the computational time but more significantly extends the requirement for measurements in the frequency range from 2.0 to 3.0 GHz.

It would be informative to compare the above algorithms with more traditional ones, for example Levenberg–Marquardt, see e.g., [1, Section 9.4.1] for an application to an inverse problem of optical tomography. This topic, however is outside of the scope of this paper. The authors hope to develop comparisons with other methods in a later work.

6. Summary

Two inverse problem methods have been proposed to recover the locations and properties (coefficient values) of interior targets from measured or simulated backscattered boundary data where the application problem is modeled by the Helmholtz equation. One of these, the p-method, was originally introduced in [16], and has a applicability restriction related to the loss tangent (see Section 2.1). The other, the H-method, which does not depend on this restriction, was introduced here for the first time allowing comparisons to be made between the properties of the two methods. This method also has the advantage of being simpler and easier to program than previous versions. The successful introduction of the H-method has provided new insights as to what is of critical importance in the previously published ESM [18,19]: not only are the treatment of incomplete boundary data and the order of the system simplified, but it is now seen that what was previously considered to be a key step, the elimination of the unknown perturbation though differentiation (in this case by frequency) is no longer required. It is this finding that extends the previous work by dropping the requirement that the loss tangent (2.2) must be independent of the frequency.

In both methods the inverse problem required the solution of a sequence of overdetermined discretized systems. The matrix systems depended only on frequency and changed slowly with respect to frequency. The significant size of these problems motivated the development of a high quality preconditioning technique for the application of the preconditioned conjugate gradient method. It was found that, for the examples of this paper, selecting one centered system for factorization as a preconditioner for every 10–12 frequencies was sufficient to give convergence on an average of 4–5 iterations. A general algorithm was developed for switching from one preconditioner to the next, and selecting the frequency at which it would be evaluated. The underlying factorization used the very efficient nested dissection method [12], with the calculations generalized to complex arithmetic.

A study was made of the frequency spacing and upper frequency required of the two methods for a single target example. It was found that a frequency spacing of .02 GHz was satisfactory for both methods. The H-method required data only up to 2 GHz, but the p-method required measurements up to 2.5 or 3.0 GHz. The effect of noise in the data was tested for both methods and it was found that a $\sigma = 0.1$ of multiplicative Gaussian noise had little effect on the results. Applications were made to both single and multitarget cases corresponding to targets filled with TNT in wet soil. While the calculations currently are too time consuming for real time evaluation, it is hoped that in a potential application to the identification of land mines they might lead to a diagnostic type procedure to reduce the large number of false positives. The computed results were accurate both in location and value for both methods with some differences. In comparing the two methods we noted that the p-method was more accurate for the extreme value in the single target case, while the H-method gave better vertical target widths and locations, required fewer frequency measurements and sometimes fewer sweeps, was faster to compute, was easier to implement and was more general.

Acknowledgements

We thank the referees for their helpful comments.

References

[1] S. Arridge, Optical tomography in medical imaging, Topical review, Inverse Problems 15 (1999) R41.

[2] C. de Boor, A Practical Guide to Splines, Springer, New York, 1978.

[3] P.L.T. Brian, A finite-difference method of high-order accuracy for the solution of three-dimensional transient heat conduction problems, AIChE J. 1 (1961) 367.

[4] M. Cheney, D. Isaacson, Inverse problems for a perturbed dissipative half-space, Inverse Problems 11 (1995) 865.

[5] M. Cheney, J.H. Rose, Three-dimensional inverse scattering for the wave equation: weak scattering approximation with error estimation, Inverse Problems 4 (1988) 435.
[6] L.M. Delves, J.L. Mohamed, Computational Methods for Integral Equations, Cambridge University Press, Cambridge, 1985.
[7] Dielectric Constant and Loss Tangent of Explosives, Data from U.S. Army Belvoir RD&E Center (unpublished).
[8] J.J. Dongarra, I.S. Duff, D.C. Sorensen, H.A. van der Vorst, Numerical Linear Algebra for High-Performance Computers, SIAM, Philadelphia, 1998.
[9] O. Dorn, H. Bertete-Aguirre, J.G. Berryman, G.C. Papanicolaou, A nonlinear inversion method for 3D electromagnetic imaging using adjoint fields, Inverse Problems 15 (1999) 1523.
[10] O. Dorn, E.L. Miller, C.M. Rappaport, A shape reconstruction method for electromagnetic tomography using adjoint fields and level sets, Inverse Problems 16 (2000) 1119.
[11] I.S. Duff, Sparse numerical linear algebra: direct methods and preconditioning, in: I.S. Duff, G.A. Watson (Eds.), The State of the Art in Numerical Analysis, Oxford University Press, Oxford, 1997.
[12] A. George, J.W.-H. Liu, Computer Solution of Large Sparse Positive Definite Systems, Prentice-Hall, Englewood Cliffs, New Jersey, 1981.
[13] G.H. Golub, C.F. Van Loan, Matrix Computations, The John Hopkins University Press, Baltimore, 1996.
[14] Y.A. Gryazin, M.V. Klibanov, T.R. Lucas, GMRES computation of high frequency electrical field propagation in land mine detection, J. Comp. Phys. 158 (2000) 98.
[15] Y.A. Gryazin, M.V. Klibanov, T.R. Lucas, Imaging the diffusion coefficient in a parabolic inverse problem in optical tomography, Inverse Problems 15 (1999) 373.
[16] Y.A. Gryazin, M.V. Klibanov, T.R. Lucas, Numerical solution of a subsurface imaging inverse problem, SIAM J. Appl. Math. 62 (2001) 664.
[17] W.H. Hayt, Engineering Electromagnetics, third ed., McGraw Hill, New York, 1974.
[18] M.V. Klibanov, T.R. Lucas, Numerical solution of a parabolic inverse problem in optical tomography using experimental data, SIAM J. Appl. Math. 59 (1999) 1763.
[19] M.V. Klibanov, T.R. Lucas, R.M. Frank, A fast and accurate imaging algorithm in optical/diffusion tomography, Inverse Problems 13 (1997) 1341.
[20] F. Natterer, F. Wuebbeling, A propagation–backpropogation method for ultrasound tomography, Inverse Problems 11 (1995) 1225.
[21] Y. Saad, M.H. Schultz, GMRES: A generalized minimal residual algorithm for solving nonsymmetric linear systems, SIAM J. Sci. Stat. Comput. 7 (1986) 856.
[22] Y. Saad, Iterative Methods for Sparse Linear Systems, PWS Publishing Co., Boston, 1996.